Please cite the Published Version

Wang, Lei, Peng, Hongjie, Lamaison, Sarah, Qi, Zhifu, Koshy, David M, Stevens, Michaela Burke, Wakerley, David, Zamora Zeledón, José A, King, Laurie A, Zhou, Lan, Lai, Yungchieh, Fontecave, Marc, Gregoire, John, Abild-Pedersen, Frank, Jaramillo, Thomas F and Hahn, Christopher (2021) Bimetallic effects on Zn-Cu electrocatalysts enhance activity and selectivity for the conversion of CO2 to CO. Chem Catalysis, 1 (3). pp. 663-680. ISSN 2667-1093

DOI: https://doi.org/10.1016/j.checat.2021.05.006

Publisher: Elsevier BV

Version: Accepted Version

Bimetallic Effects on Zn-Cu Electrocatalysts Enhance Activity and Selectivity for the Conversion of CO_2 to CO

Lei Wang[1,2‖], Hongjie Peng[3‖], Sarah Lamaison[1,4‖], Zhifu Qi[1,5], David M. Koshy[1], Michaela Burke Stevens[1], David Wakerley[1], José A. Zamora Zeledón[1], Laurie A. King[6], Lan Zhou[7,8], Yungchieh Lai[7], Marc Fontecave[4], John Gregoire*[7,8], Frank Abild-Pedersen*[3], Thomas F. Jaramillo*[1,3], and Christopher Hahn*[3,9]

[1] SUNCAT Center for Interface Science and Catalysis, Department of Chemical Engineering, Stanford University, California 94305, United States

[2] Department of Chemical and Biomolecular Engineering, National University of Singapore, Singapore 117585, Singapore

[3] SUNCAT Center for Interface Science and Catalysis, SLAC National Accelerator Laboratory, Menlo Park, California 94025, United States

[4]Sorbonne Universités, Collège de France, Laboratoire de Chimie des Processus Biologiques, CNRS UMR 8229, 75231 Paris, France

[5] Zhejiang Energy Technology Research Institute Co. Ltd, Hangzhou, Zhejiang 311121, China

[6] Faculty of Science and Engineering, Manchester Metropolitan University, Manchester M1 5GD, U.K

[7] Joint Center for Artificial Photosynthesis, California Institute of Technology, Pasadena, California, 91125, United States

[8] Division of Engineering and Applied Science, California Institute of Technology, Pasadena, California 91125, United States

[9] Materials Science Division, Lawrence Livermore National Laboratory, Livermore, CA 94550, USA.

‖These authors contributed equally to this work

Correspondence: hahn31@llnl.gov, jaramillo@stanford.edu, abild@slac.stanford.edu, gregoire@caltech.edu.

Summary: We report an active Zinc-Copper (Zn-Cu) bimetallic electrocatalyst for CO_2 reduction to CO, prepared by a facile galvanic-procedure. Under moderate overpotentials, Zn-Cu alloys that are Zn-rich exhibit intrinsic activity for CO formation superior to that of pure Zn, Cu, and Ag, the latter of which is the state-of-the-art catalyst in CO_2 electrolyzers. Combinatorial experiments involving catalysts prepared by physical vapor deposition reveal trends across the Zn-Cu alloy system, corroborating the high CO selectivity unrivaled by other alloys and intermetallics. A combination of physical and electrochemical characterization and first principles theory reveals that the origin of this synergy in intrinsic activity is an electronic effect from bimetallic Zn-Cu sites that stabilizes the carboxyl intermediate during CO_2 reduction to CO. Furthermore, by integrating Zn-Cu into gas-diffusion-electrodes we demonstrate that the bimetallic effects lead to improved electrocatalytic performance at industrially relevant currents. These insights provide catalyst design principles that can guide future development of efficient and earth abundant CO-producing electrocatalysts.

Keywords: CO_2 reduction, CO formation, bimetallic effect, electrocatalysis

Introduction

Syngas, a fuel gas mixture consisting primarily of CO and H_2, is one of the most important resources in the chemical industry as a precursor for many products including high energy density fuels, *e.g.* methanol, ammonia and synthetic petroleum.[1] Active research on converting syngas to higher alcohols through either thermal or biocatalytic processes are expected to further boost the syngas industry.[2,3] As the majority of syngas is currently produced from fossil fuels,[4] it would be of great value to establish sustainable pathways to CO and H_2. One such route for generating CO is electrochemical CO_2 reduction (CO_2R), where CO_2, H_2O, and renewable electricity can be used to upgrade CO_2 into CO. This is a promising strategy to mitigate CO_2 emissions by developing a carbon industry based on CO_2 that stores variable electricity from renewable sources in chemical form.[5–7]

Establishing catalyst design principles for maximizing selectivity and activity towards desired products is crucial for the industrialization of electrochemical CO_2R. Many successful strategies that have been reported for developing high-performance CO-production catalysts including nano-structuring state-of-the-art Au and Ag catalysts,[8–13] combining metals into multimetallic electrocatalysts,[14-24] incorporating first row transition metals into heteroatom-doped graphitic carbons,[25–31] and immobilizing molecular catalysts onto electrode surfaces.[32–35] As shown in Fig. 1, precious metal Au- and Ag-based materials remain as the most active electrocatalysts for CO_2R to CO, motivating the development of new catalysts comprised of earth abundant metals. In addition to their high intrinsic activity and selectivity for CO production, nano-structuring Au and Ag materials has been shown as a promising strategy to further improve their geometric activities by leveraging a combination of surface area effects,[36] local pH[11] and field effects.[9] However, normalizing the geometric activities of nanostructured Au and Ag electrodes to their corresponding electrochemically active surface areas (ECSA), similar or even lower activities are obtained in comparison to those of planar Au and Ag foils, suggesting that increasing their electrode surface areas does not improve intrinsic activities. Transition metals and nitrogen doped carbons (M-N-C) have also been extensively studied as CO producing catalysts.[51-56] An important area of study is identifying and quantifying the active sites due to substantial heterogeneity of these materials with many distinct, isolated motifs. Efforts to understand these factors are critical to overcome the generally low density of active sites of M-N-C type materials and to make them competitive to the precious metal catalysts on an electrode area basis. Molecular catalysts are known to have high turnover frequency (TOF) per site for reducing CO_2 to CO, *e.g.* a TOF ~ 10^4 has been observed for a Fe-porphyrin catalyst at overpotential of 0.56 V.[37] After immobilized to conductive substrate, molecular catalysts behave similarly to the M-N-Cs, which is expected due to the similarity of their active motifs.[33–35] Understanding how the intrinsic activity of the molecular catalyst is affected by heterogenization to the solid-electrolyte interface remains a significant research challenge.[38]

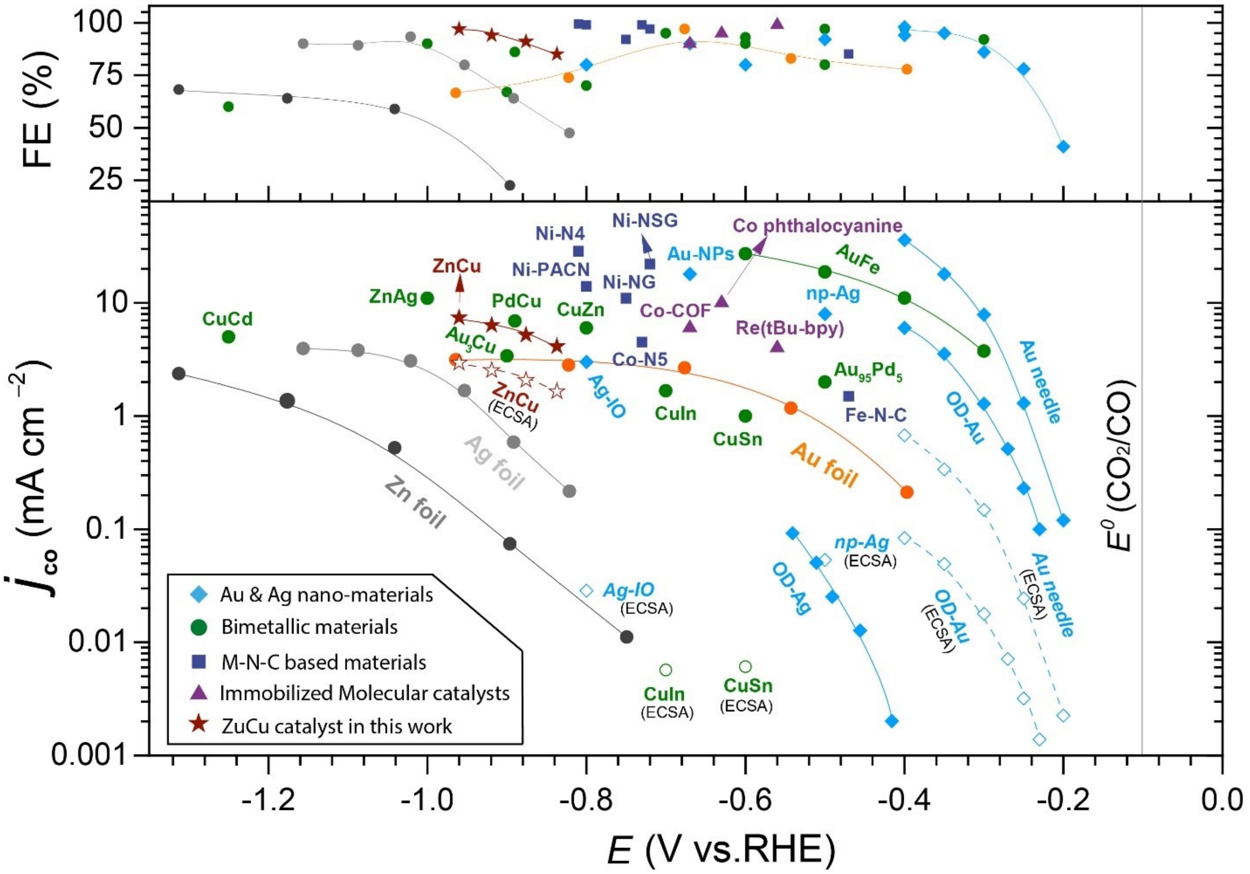

Figure 1. **Electrocatalytic performance of various materials for aqueous CO_2R to CO under neutral pH.** Using planar Au-, Ag- and Zn-based catalysts as references, four different types of materials are categorized: Au and Ag nano-materials (Au needles;[9] OD-Au;[8] Au-NPs;[12] np-Ag;[13] OD-Ag;[11] Ag-IO[10]); bimetallics (AuFe;[18] $Au_{95}Pd_5$;[14] Au_3Cu,[21] PdCu;[17] CuSn;[20] CuIn;[16] CuZn;[22] ZnAg;[19] CuCd[23]); metal- and nitrogen-doped carbon materials (M-N-C) (Ni-NG;[26] Ni-NSG;[30] Ni-

N_4;[27] Ni-PACN;[28] Fe-N-C;[25] FeN_4;[31] Co-N_5;[29]) and immobilized molecular catalysts (Re(tBu-bpy);[35] Co-COF;[33] Co phthalocyanine[34]). Solid symbols represent the geometric current densities, hollow symbols represent the ECSA-normalized current densities (if reported). Data points were adapted from corresponding literatures (Supplementary Table 1-2). All catalysts were tested in H-type cells or equivalents under aqueous conditions. The Cu-based catalysts are all highly selective for CO, with only H_2 and formate as major by-products.

By mixing metals at the atomic level, *e.g.* through alloying, solid solutions, intermetallic and segregated phases, the electronic properties of the resulting metallic surfaces can be modified and tuned to facilitate CO formation. Thus, bimetallic materials based on non-precious metals are promising for replacing the state-of-art Au- and/or Ag-based catalysts. In fact, several studies have demonstrated synergistic bimetallic effects for CO formation, showing enhanced activity with respect to the sum of their monometallic catalysts.[14,24] However, clear demonstrations of improving the intrinsic activity for CO_2R to CO through bimetallic effects among non-precious metal catalysts are rare. Thus, further probing and understanding mechanisms among bimetallic catalysts are needed to establish structure-performance relations, which can ultimately lead to improved intrinsic activity that is comparable or higher than that of precious Au- and/or Ag-based catalysts. As Zn is the only non-precious material in the group of CO-producing monometals it is a promising candidate for bimetallic studies.[39] However, Zn has a lower intrinsic activity and selectivity for CO_2R to CO compared to Au and Ag (Fig. 1),[39–41] which is likely related to the weak CO binding energy on Zn surfaces.[40,42] As Cu has a moderate CO binding energy which is higher than that of Zn, incorporating Cu into Zn could, in principle, increase the CO binding energy of the bimetallic surface, and potentially upgrade its CO_2R performance.[40] Previous efforts have shown that bimetallic alloys of Zn_xCu_{1-x} (Zn-Cu) that are Zn-rich are selective towards syngas (CO and H_2),[22] while those that are Cu-rich favor > $2e^-$ products.[43–46] These promising results motivate further studies to understand whether alloying Zn and Cu enhances the bimetallic's intrinsic activity for CO_2R to CO, and the specific atomic-scale interactions between Zn and Cu (*e.g.*, ligand and strain effects) that engender improved catalytic performance.

In this work we prepare Zn-Cu catalysts in a different manner, exploiting a galvanic exchange procedure to synthesize a planar Zn-Cu bimetallic catalyst with relatively high surface Zn to Cu ratio that is highly selective for CO_2R to CO. Synchrotron X-ray absorption spectroscopy demonstrates that incorporating Cu engenders an electronic effect that transfers outer shell electron density from Zn to Cu. We hypothesize that this electronic effect is responsible for the observed synergistic catalytic activity of Zn-Cu for CO_2R to CO, which is greater than that of pure Cu or Zn. Density functional theory (DFT) calculations suggest that the bimetallic promotes the overall reaction rate towards CO formation by stabilizing the carboxyl (COOH*) intermediate. We used the same galvanic exchange procedure to implement powder-based Zn-Cu onto a gas diffusion electrode (GDE), and demonstrate that the catalyst is active and selective for CO_2R to CO at industrially relevant current densities in a vapor-fed device. The design principles and insights resulting from this work can guide the future development of earth abundant catalysts for CO_2 electrolyzers.

Results and Discussion

Synthesis and characterization of Zn-Cu bimetallic electrocatalysts. The Zn-Cu electrodes were prepared by immersing pre-polished polycrystalline Zn foils into a dilute $CuSO_4$ solution at room temperature for a short period of time (referred to Zn-Cu (ns) electrodes, ns denotes time as 1, 5, 30, and 60 seconds). There is an obvious visual change upon deposition as the sample changes from silver to black in color. A representative scanning electron microscope (SEM) image of the Zn foil before and after 5 seconds of the galvanic exchange is shown in Fig. 2a and 2b, respectively. Notably, a layer of nanoparticles (50-100 nm in size) is seen to form on the surface of Zn foil from this rapid treatment (Fig. 2b), indicating that the galvanic exchange procedure rapidly roughens the surface of Zn during the process. X-ray photoelectron spectroscopy (XPS) analysis suggests that the surfaces of these nanoparticles are enriched in Zn with a Zn:Cu ratio of ~10:1 (Supplementary Fig. 1). A comparison of SEM and XPS data for 1, 5, 30, and 60 seconds Zn-Cu electrodes indicates that Cu composition and nanoparticle size increase concomitantly with the reaction time (Supplementary Fig. 2). We propose that the surface roughening results from rapid Zn crystal deformation, starting from the grain boundaries and defects, likely due in part to the large thermodynamic driving force of the galvanic reaction ($E^0_{Cu^{2+}/Zn}$ =1.1 V).[47,48] Grazing incidence X-ray diffraction (XRD) was performed (Supplementary Fig. 3) to assess the crystallinity of the prepared samples. No new XRD patterns emerged nor were expected for Zn-Cu bimetallic formation, due to a combination of the rough electrode-surface which will introduce significant amount of bulk-Zn signals even for grazing incidence configuration, and the similarity of the XRD patterns for Zn and Zn-Cu alloys that are Zn-rich.[44] The absence of a pure Cu-metal phase, however, indicates a bimetallic surface without major phase separation. Atomic force microscopy (Supplementary Fig. 4) was introduced to directly measure the surface area differences between the Zn-Cu electrodes and the planar Zn foil-based electrode. In addition, double layer capacitance measurements (Supplementary Fig. 5) were also introduced to measure the increase in double layer capacitance of Zn-Cu compared to that of Zn foil, since it should scale with the electrochemical active surface area. Increase of 1.35 and 2.5 times in surface area were obtained for Zn-Cu electrode by the above two different measurements, respectively. Thus, while the galvanic exchange procedure nanostructures the surface, we conclude that it leads to relatively minor changes in the porosity of the electrodes.

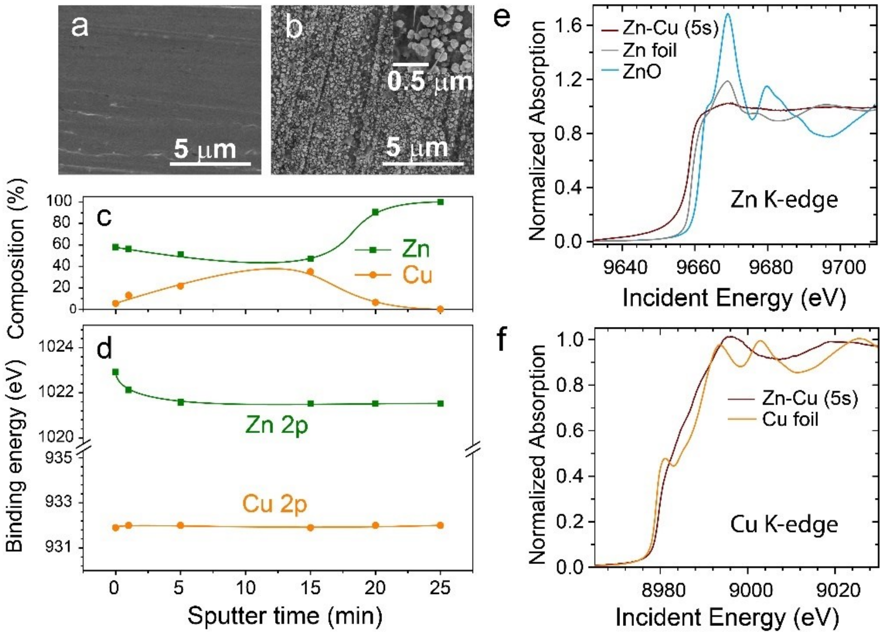

Figure 2. Physical characterization of the Zn-Cu bimetallic surface. SEM of Zn foil before (a) and after (b) galvanic exchange for 5 seconds in 10 mM $CuSO_4$. XPS sputter depth profiling of the Zn-Cu (5s): (c) the surface compositions of Zn and Cu as a function of sputtering time, the balance of elements is oxygen. (d) the *2p3/2* peak positions of Zn and Cu at different sputtering times. The sputtering rate is ca. 1 nm/min. XAS spectra: Normalized Zn K-edge (e) and Cu K-edge (f) X-ray absorption spectra for Zn-Cu (5s); Zn foil, ZnO and Cu foil are provided as references.

Electronic interactions between Zn and Cu in the near-surface region of Zn-Cu bimetallics. The Zn-Cu (5s) electrode was probed with XPS to investigate its surface composition and electronic structure. The presence of XPS peaks at binding energies of 1022.5 (Zn 2*p*3/2) and 1045.5 eV (Zn 2*p*1/2) indicates that ZnO is present in the as prepared sample. As Zn metal is readily oxidized by air to form a native oxide layer ($\Delta_f G^\circ_{ZnO} = 320.5$ kJ mol^{-1}),[49] we suggest that ZnO forms from oxygen exposure prior to the *ex situ* XPS measurement. This oxidation process is more rapid when the surface consists of nanoparticles,[50] which are present on the Zn-Cu samples in our work. Based on Pourbaix analysis of Zn,[49] we suggest that the native oxide is reduced to Zn metal under CO_2R conditions. This hypothesis is in agreement with recent *ex situ* and *operando* characterization studies[51,52] that indicate metallic Zn is the active phase for electrochemical CO_2R. On the other hand, Cu is likely in its metallic state in a Zn-Cu alloy (*vide infra*), as only a Cu 2*p*3/2 peak was observed at a downshifted binding energy of 932.0 eV with a notable absence of satellite peaks for both CuO and Cu_2O, and about ~1 eV lower than that of pure Cu metal.[53] This suggests a strong ligand effect from neighboring Zn atoms, further below we describe our efforts involving X-ray absorption spectroscopy (XAS) to further probe electronic structure. XPS depth profiling using argon sputtering shows that both the Zn/Cu ratio and the Zn 2*p*3/2 peak position are dependent on the sputter time (Fig. 2c, d, Supplementary Fig. 6). We hypothesize that the trend of Zn surface segregation arises because Zn is more oxophilic than Cu, which is commensurate with the aforementioned conclusion that ZnO is present on the surface. Conversely, the Cu *2p*3/2 peak position is consistent at ~932.0 eV, suggesting that the electronic structure of Cu is similar throughout the probe depth.

To further investigate these electronic interactions, we performed synchrotron XAS on the Zn and Cu K-edge within both their near-edge structure (XANES, Fig 2e, d) and extended X-ray absorption fine structure (EXAFS) regions (Supplementary Fig. 7) for the Zn-Cu (5s) electrode. Zn K-edge XANES reveals no prominent pre-edge feature for Zn-Cu (5s) with a lower edge energy of 9658.7 eV compared to 9659 eV for the Zn foil reference, suggesting that Zn within the Zn-Cu (5s) electrode is mainly in a reduced state. Although XPS results indicate that ZnO is present on the surface of Zn-Cu (5s), ZnO features were not observed in the XANES data for Zn-Cu (5s); we attribute the lack of ZnO features in the XANES data to the large XAS probe depth (~ 1 µm) relative to the thin ZnO layer (<5-10 nm). Analysis of the Zn K-edge EXAFS region corroborates this conclusion, as there is a single scattering peak at 2.25 Å that is consistent with Zn-Zn metal bonding (Supplementary Fig. 7). Notably, the Cu K-edge XANES of Zn-Cu (5s) shows substantially different features relative to those of the Cu foil reference. In particular, the pre-edge peak at ~8981 eV that is prominent for the Cu foil is greatly suppressed for Zn-Cu (5s). Based on the calculated projected density of states (PDOSs) for Zn 4*s* and Cu 4*s* orbitals in Zn-Cu (5s) (Supplementary Fig. 8), we attribute this phenomenon to Zn donating 4*s* electron density to neighboring Cu atoms, which is in agreement with conclusions from previous studies on Zn-Cu alloys.[54] Similar to the XPS results, the Cu K-edge EXAFS data shows a single peak at 2.25 Å indicating that Cu is in a primarily metallic state (Supplementary Fig. 7). All the above evidence demonstrates that the galvanic exchange process generates a well-mixed bimetallic system instead of a Cu layer on top of the bulk Zn metal. Moreover, there are strong electronic interactions between Zn and Cu atoms in the Zn-Cu (5s) bimetallic, exhibiting distinct electronic properties in comparison to those of pure Zn and Cu.

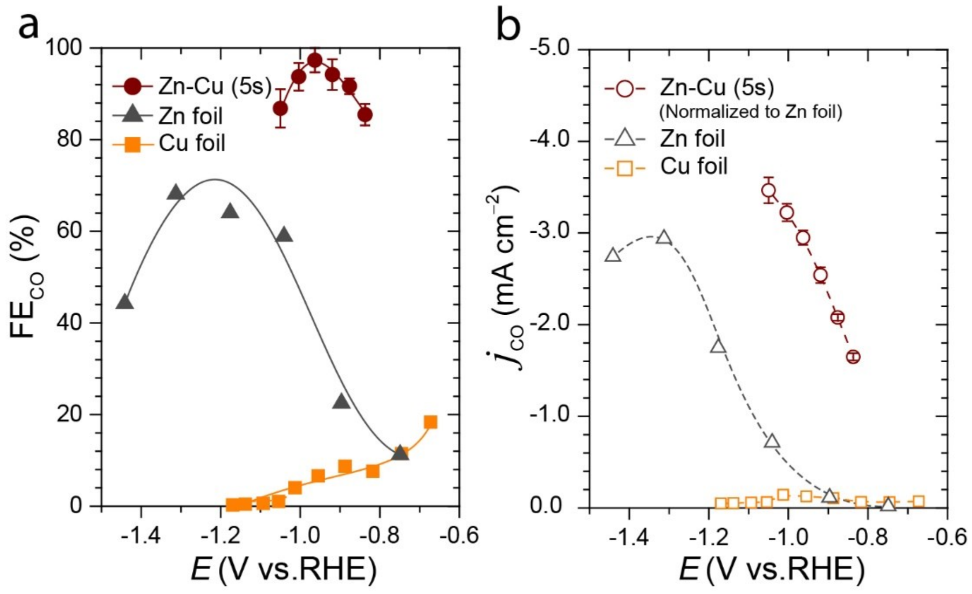

Figure 3. **CO_2R by Zn-Cu (5s) bimetallic catalysts and its performance comparison to pristine Zn and Cu.** Faradaic efficiencies (FE) and normalized partial current densities for CO formation on the Zn-Cu (5s) bimetallic electrode and literature data for Zn and Cu electrodes,[40] as a function of the applied potential. Data points for Zn-Cu (5s) are averaged from three individual measurements. The only other measured products are H_2 and formate (Supplementary Table 3).

Electrocatalytic performance of Zn-Cu bimetallic electrodes. The electrocatalytic CO_2R performance of the Zn-Cu electrodes were evaluated using 0.1 M $KHCO_3$ as the electrolyte in a two-compartment electrochemical cell. We first investigated how the surface concentration of Cu in Zn-Cu affects the CO_2R activity by using a combination of cyclic voltammetry (CV) and chronoamperometry (CA) measurements to evaluate the 1, 5, 30, and 60 seconds Zn-Cu electrodes. The results indicate that the CO_2R to CO activities do not scale linearly with the surface Cu concentration, and instead plateau after 5 seconds of the galvanic exchange treatment (Supplementary Fig. 9). Thus, for the remainder of this work we used the Zn-Cu (5s) electrode as a platform for a deeper investigation of CO_2R activity and selectivity.

To determine whether incorporating Cu into Zn enhances the intrinsic catalytic activity, we compared the electrocatalytic performance of Zn-Cu (5s) to that of pure Zn and Cu. Initial CV measurements suggest that Zn-Cu (5s) electrode has a higher current density compare to pristine Zn and Cu electrodes under the same CO_2R catalytic condition (Supplementary Fig. 10), motivating more detailed CA measurements with product quantifications to confirm the increase in current density is a result of enhancement in CO_2R activity. As the galvanic exchange procedure induces nanostructuring of Zn-Cu (5s), we accounted for differences in the surface area of the electrodes by normalizing partial current densities to several metal foil-based electrodes (Zn, Ag, Au) and employing several different surface area measurements (Supplementary Fig. 4, Fig 5, Note 1). At the same electrode potential (–0.96 V vs. RHE) Zn-Cu (5s) is almost fully selective (97% FE) for the CO pathway, whereas Zn is only 30% selective (FE) (Fig. 3a). Formate and hydrogen are minor products evolved from Zn-Cu; no additional products were detected (Supplementary Table 3). The normalized data indicates that Zn-Cu (5s) is 7 times more active than pure Zn for CO_2R to CO at an electrode potential of –0.96 V *vs.* RHE (Fig. 3b). The above results indicate that Zn-Cu (5s) is more selective than Zn for CO_2R to CO by improving both the intrinsic catalytic activity for the CO_2R to CO pathway and suppressing the competing HER. To compare the intrinsic catalytic activities of Zn-Cu (5s) and Cu, we analyzed the normalized total CO_2 consumption rates to account for the fact that Cu is more selective for further reduced products beyond CO (Supplementary Fig. 11). This assessment clearly demonstrates that Zn-Cu (5s) has a faster CO_2R rate than pure Cu and Zn regardless of which product is being formed from CO_2, indicating that incorporating Cu into Zn engenders a synergistic effect that improves the intrinsic CO_2R activity of Zn-Cu bimetallic beyond that of either of its component metals.

Since previous research has shown that nanostructuring CO_2R electrocatalysts can also induce changes in selectivity through porosity effects,[55] we further investigated trends in reactivity using sputtered thin films of Zn-Cu with negligible surface roughness, since the thin-film based electrodes are reasonable approximation to the galvanic exchanged system due to their similar surface Zn:Cu ratio. A comparison of sputtered $Zn_{10}Cu_1$ and Zn films across a range of electrode potentials shows similar trends in activity and selectivity as those described above for the Zn-Cu (5s) and Zn foils (Supplementary Fig. 14). For example, the $Zn_{10}Cu_1$ film in comparison to the Zn film exhibits significantly improved intrinsic activity and selectivity for CO_2R to CO and suppressed intrinsic activity and selectivity for the HER. These results corroborate our conclusion that the aforementioned synergy in intrinsic activity is likely due to a bimetallic effect rather than an electrode surface area effect. To better understand the impact of the electrode composition on reactivity, we also prepared and tested Zn_1Cu_{10} thin films to reflect the other extreme of a high Cu:Zn ratio for the sake of comparison. While these Zn_1Cu_{10} films show similar partial current densities for CO formation as those for $Zn_{10}Cu_1$ films, the Zn_1Cu_{10} films are also more active and selective for the HER and for > 2 e^- CO_2 reduction products, more similar to pure Cu. Thus, the results indicate that a Zn-rich surface is more favorable for applications that require high selectivity for CO_2R to CO.

To assess a broader range of Zn-Cu bimetallic compositions, the study of sputtered films was extended to a composition library in which 5 compositions spanning 4% to 70% Zn were synthesized. These films were examined for CO_2R at −0.85 V vs RHE using a specialized high throughput electrochemical recirculation cell, enabling product distributions to be assessed after only 15 min. of electrolysis. The results are shown in Supplementary Fig. 15 and demonstrate that the intrinsic activity and product selectivity vary dramatically with film composition. For lower concentrations of Zn, the HER activity increases substantially with increasing Zn concentration up to approximately 50%, reaching a current density of 13.5 mA cm^{-2} corresponding to a Faradaic efficiency of over 83% for H_2. Further increasing in Zn concentration from 50% to 70% results in more than 10-fold decrease in H_2 partial current density and more than 10-fold increase in CO partial current density. These trends continue with increasing Zn concentration to the $Zn_{10}Cu_1$ catalyst noted above, which exhibits catalyst selectivity beyond that observed in any of the other alloy compositions. This maximum in CO selectivity coincides with the formation of an hcp alloy in the sputter deposited films, as was observed with the galvanic exchange catalysts discussed above. The collective results involving Zn-Cu catalysts, prepared in various ways across a range of compositions and investigated in multiple laboratories, robustly demonstrate the unique catalytic properties of Cu alloyed in hcp Zn. This motivates theoretical investigations of the selectivity-enhancing mechanisms involved.

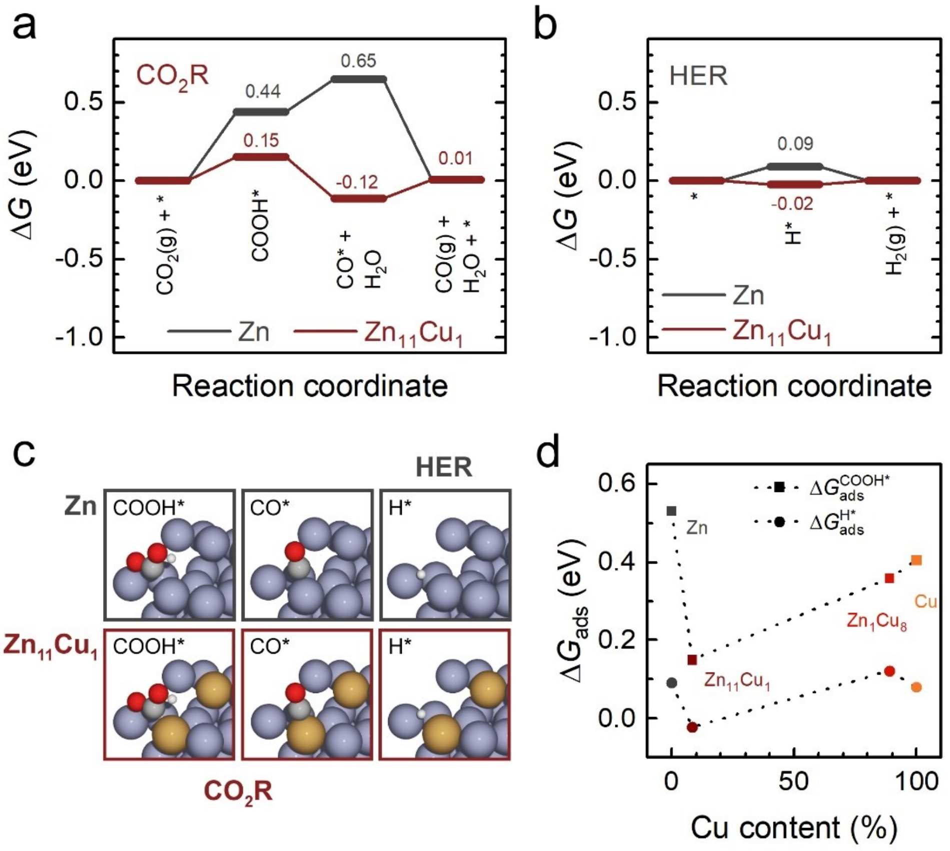

Figure. 4. DFT calculations. Free energy diagrams of (a) CO_2R to CO (1 μbar) and (b) HER on clean stepped *hcp* Zn(100) and *hcp* $Zn_{11}Cu_1$(100) surfaces at 0 V *vs.* RHE. Each reduction step is assumed to proceed through transferring a proton-electron pair to the surface species. The potential of 0 V vs. RHE is set to clearly show the PDS rather than reflecting the actual CO_2R condition. (c) Optimized atomistic configurations showing the adsorption of key intermediates (COOH* and CO* for CO_2R; H* for HER) on the surfaces. Purple grey, dark yellow, grey, red, and white spheres refer to Zn, Cu, C, O and H atoms, respectively. (d) Adsorption free energies (ΔG_{ads}) of COOH* and H* on step sites as a function of the compositional fraction of Cu in the near-surface (top two) layers of different catalytic surfaces, where Zn_1Cu_8 and Cu are in the *fcc* crystal structure.

Theoretical insights on the impact of bimetallic effects on surface reactivity. The above experimental (Fig. 2) and computational (Supplementary Fig. 6) results on Zn-Cu alloys suggest that the observed synergy in activity is related to an electronic effect between Zn and neighboring Cu atoms that affects the adsorption of key reaction intermediates. To further gain insight into this enhancement in performance, we carried out theoretical simulations based on density functional theory (DFT). Since undercoordinated sites have been identified as the major active sites for CO_2R to CO,[56] we therefore evaluated reaction energetics for both CO_2R and the competing reaction HER, on stepped surfaces of Zn-Cu alloys with different surface compositions (see details in the Computational Details and Supplementary Fig. 16). The CO_2R mechanism is considered to proceed through the sequential two-step reduction of an adsorbed CO_2 to COOH* and then to CO* and water, followed by the desorption of CO (Fig. 4a), while a Volmer–Heyrovsky mechanism is considered for HER (Fig. 4b). Fig. 4a shows that the potential determining step (PDS) is the first protonation step to form COOH*. The $Zn_{11}Cu_1$ surface possesses a stronger COOH* adsorption energy ($\Delta G_{\mathrm{ads}}^{\mathrm{COOH*}}$) by 0.15 eV compared to that of the pristine Zn (0.44 eV), which can explain the earlier onset potential for CO production on the Zn-Cu (5s) electrode. At sufficiently negative potentials (*e.g.,* −0.96 V vs. RHE), both CO formation and HER become thermodynamically favorable (Supplementary Fig. 17). The suppression of the HER in Zn-Cu (5s) is also explained by the computational modeling. On one hand, surface H* is stabilized by incorporating Cu into Zn which should in principle improve HER activity, however, this is not the case for two reasons. First, this effect is not as profound as that for COOH*, indicating a smaller effect on the HER than for the CO_2R (Fig. 4b). Secondly, CO-poisoning can have a substantial impact on H-binding and on the resulting HER activity.[57] At high CO coverages, the H* is actually weakened substantially during true operating conditions, an effect that suppresses the HER activity of Zn-Cu more so than with Zn (Supplementary Fig. 18). As revealed by the binding configurations, the two metals of the Zn-Cu site synergistically contribute to the COOH* stabilization through Cu-C and Zn-O coordination, respectively (Fig. 4c). CO and OH adsorption energies on individual Zn and Cu sites demonstrate the relatively stronger carbophilicity of Cu and stronger oxophilicity of Zn (Supplementary Fig. 19). Similarly, the Zn-Cu dual site in Zn_1Cu_8 also has a more negative $\Delta G_{\mathrm{ads}}^{\mathrm{COOH*}}$ than the monometallic Cu site (Fig. 4d and Supplementary Fig. 20). This is in agreement with the experimental results (Supplementary Fig. 14): an enhanced CO formation activity is observed on the Cu-rich Zn-Cu surface, while retaining the Cu-like ability for further reduction of CO into multi-carbon products. The $\Delta G_{\mathrm{ads}}^{\mathrm{COOH*}}$ as a function of the Zn/Cu composition displays a non-monotonic correlation (Fig. 4d) and thus demonstrates the key role of the bimetallic sites in optimizing the reaction energetics. $\Delta G_{\mathrm{ads}}^{\mathrm{COOH*}}$ and $\Delta G_{\mathrm{ads}}^{\mathrm{H*}}$ are usually used to assess the CO_2R to CO and HER activity, respectively,[58] and narrowing the difference between the two ($\Delta(\Delta G) = \Delta G_{\mathrm{ads}}^{\mathrm{COOH*}} - \Delta G_{\mathrm{ads}}^{\mathrm{H*}}$) can lead to an onset potential of CO_2R closer to that of HER. Note that the Volmer step in HER is inherently different in reaction nature from COOH formation and thus $\Delta(\Delta G)$ can only serve as a relative measurement of CO_2R-to-CO vs. HER selectivity. Deeper understanding of the factors that control selectivity necessitates sophisticated electrochemical barrier calculations. Field-stabilization of a bent CO_2* intermediate involved in COOH formation also contributes to favoring CO_2R over the HER.[59] By comparing $\Delta G_{\mathrm{ads}}^{\mathrm{COOH*}}$ and $\Delta G_{\mathrm{ads}}^{\mathrm{H*}}$ in a range of stepped metal surfaces, we find that Zn-rich $Zn_{11}Cu_1$ exhibits the smallest $\Delta(\Delta G)$ among all the weak-binding elementary metals known for catalyzing CO_2R to CO whereas strong-binding metals with even smaller $\Delta(\Delta G)$ suffer from strong CO poisoning effect that limits their CO_2R activity (Supplementary Fig. 21). CO poisoning is known to have a more profound effect on CO_2R than HER owing to the stronger lateral interaction between adsorbed CO* and CO_2R intermediates (CO* and COOH*) than H*.[60] Overall, the reduced $\Delta(\Delta G)$ from pristine Zn to $Zn_{11}Cu_1$, along with a moderate CO binding strength on $Zn_{11}Cu_1$, comprises the main mechanistic insight for the enhanced CO production activity and selectivity on bimetallic Zn-Cu (5s).

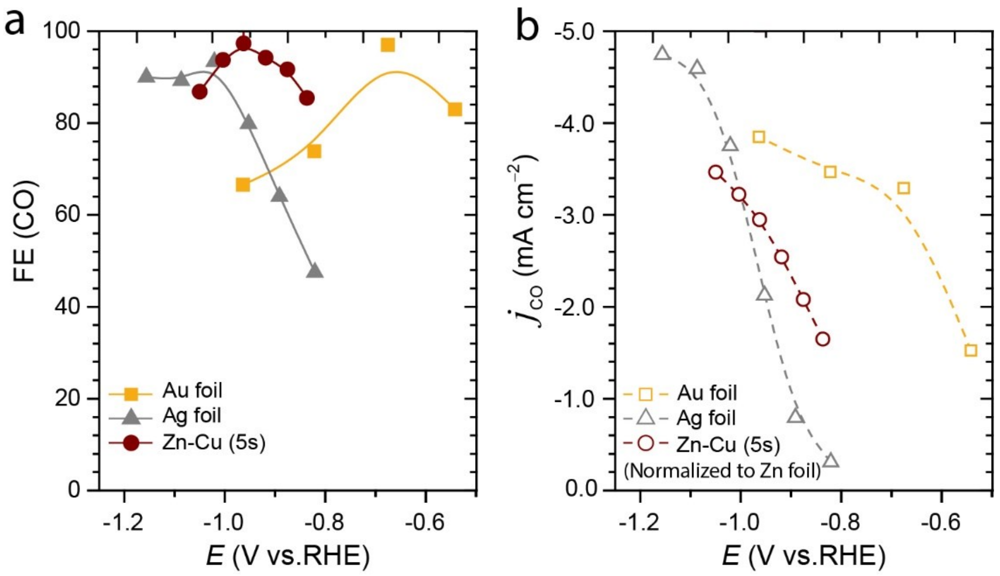

Figure. 5. CO_2R performance comparisons among galvanic prepared Zn-Cu (5s), planar Ag and Au electrodes[10]. Within a large potential window, the foil-based Zn-Cu (5s) electrode show higher selectivity for CO formation compare to foil-based Ag catalyst. Zn-Cu (5s) exhibits slightly higher CO partial current density (normalized to Zn foil by ECSA) compared to Ag foil.

Evaluating the long-term stability of Zn-Cu (5s) and its performance in comparison to precious metal catalysts. As shown by SEM and XPS data, the nanostructure and surface composition of the Zn-Cu (5s) electrode are relatively unchanged after 1 hour of CO_2R testing (Supplementary Fig. 12). Longer-term testing over 20 hours indicates that the CO production rate remains relatively stable; there is a minor decrease in selectivity for CO_2R to CO (95% to 86% FE) due an increase in the HER over time (Supplementary Fig. 13). This increase in the HER is likely due to electroplating of trace impurities (e.g. transition metals) onto the cathode over long periods. Nonetheless, this initial stability test indicates that Zn-Cu (5s) is promising for long-term application in CO_2R electrolyzes.

As we discuss above, to the best of our knowledge there has not been a previous report of an earth abundant bimetallic that has better or similar intrinsic activity for CO_2R to CO than Ag or Au, which are precious metals that are typically the major or only constituents of state-of-the-art catalysts. An analysis of CO_2R on Zn-Cu (5s), Ag, and Au foils as a function of the electrode potential demonstrates that Zn-Cu (5s) has comparable selectivity for CO production as Ag and Au (Fig. 5) and slightly improved intrinsic activity than Ag for CO_2R to CO. As COOH formation usually involves the formation of a partially charged intermediate, bent CO_2*, Au has an exceptional ability to stabilize this intermediate through strong interfacial electric fields as it has the most positive potential of zero charge among metal catalysts (Supplementary Fig. 22).[59] While Zn-Cu (5s) is less intrinsically active for CO_2R to CO than Au, these results indicate that earth abundant bimetallics could potentially serve as suitable replacements for precious metal catalysts in CO_2 electrolyzers.

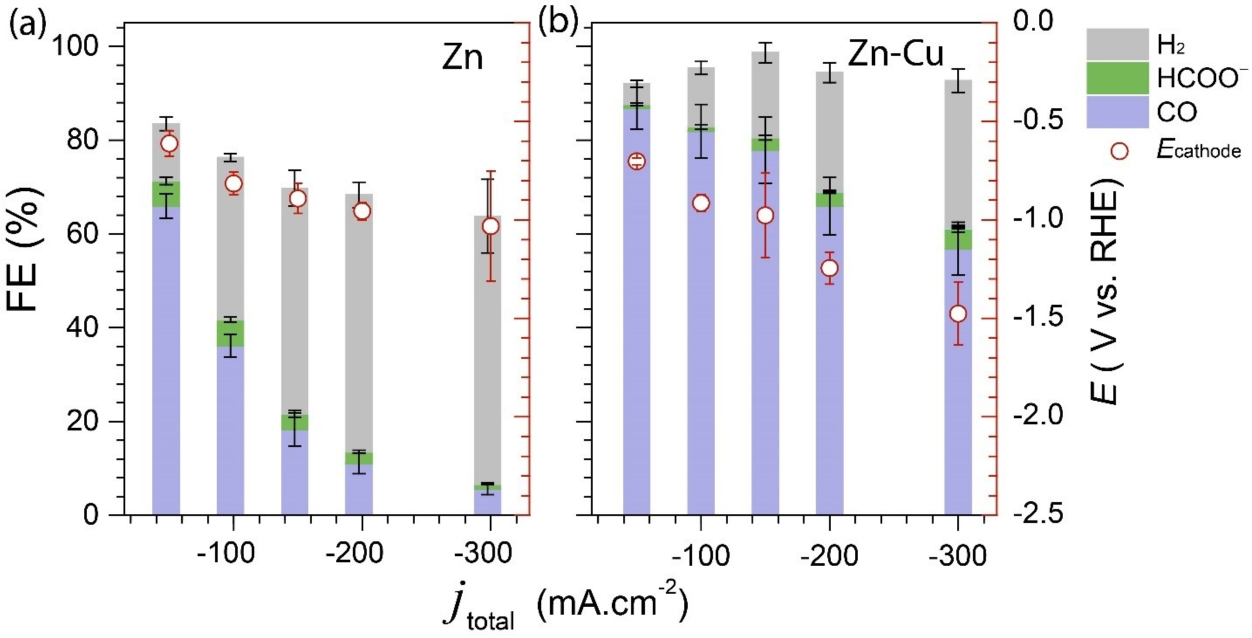

Figure. 6. **CO$_2$R in a gas diffusion electrode reactor**. Comparison of the electrocatalytic CO production of Zn (a) and Zn-Cu (powder) (b) gas diffusion electrodes for CO$_2$R, at different current densities. Electrolysis were carried out in 1.0 M KOH, circulated at 10 mL min^{-1}; CO$_2$ flow 75 sccm.

CO$_2$R to CO on Zn-Cu (powder) at high reaction rates. Based on the above insights, we integrated Zn-Cu catalysts onto gas diffusion electrodes (GDE) to evaluate their performance within a GDE reactor at industrially relevant reaction rates. Commercial Zn powder was used to prepare Zn-Cu (powder) by utilizing the same galvanic exchange procedure described above, and the particles were subsequently integrated onto GDEs to evaluate for CO$_2$R in 1.0 M KOH (more details on the reaction conditions can be found in the Methods section). A direct comparison of Zn-Cu (powder) GDEs with Zn GDEs at a given current density shows significantly enhanced CO$_2$R selectivity to CO and decreased HER selectivity for the Zn-Cu system (Fig. 6, Supplementary Table 5), commensurate with the trends described above for the planar Zn-Cu and Zn electrodes. Notably, the differences in product selectivity are more pronounced at higher current densities, demonstrating the advantages of incorporating a small amount of Cu into Zn for applications that require high total reaction rates. Although our Zn-Cu GDEs are not as performant as state-of-the-art Ag-based GDEs,[62,63] we suggest that further research to optimize the catalyst layer[62] will close this performance gap. A considerable portion of the FE is unaccounted for in the measured product distribution for the GDEs with pure Zn, indicating possible corrosion/deposition processes that take place concurrently with CO$_2$R. As Pourbaix analysis suggests that Zn is unlikely to be stable[61] under the alkaline conditions of our CO$_2$R measurements, we hypothesize that surface redox processes underpinning durability such as corrosion and deposition lead to losses in FE under these operating conditions. In contrast, nearly all the FE is accounted for with the Zn-Cu (powder) GDEs, suggesting that incorporating Cu imparts stability to Zn electrocatalysts. Future *operando* studies using synchrotron X-ray techniques could probe this dynamic reaction environment, providing insights on how to develop more robust systems under these harsh reaction conditions.

Conclusion

We present bimetallic Zn-rich Zn-Cu as a highly efficient CO_2R to CO electrocatalyst prepared by a facile galvanic procedure. The Zn-Cu catalyst exhibits dramatically improved selectivity and activity for CO formation compared to those of pristine Zn and Cu electrocatalysts, and remarkably, also shows higher intrinsic activity than a planar Ag catalyst within the operating potential window from –0.8 to –1.0 V *vs.* RHE. This enhanced intrinsic activity for CO formation on Zn-Cu catalysts is attributed to the electronic effect originating from the Cu adatoms on the Zn surface. DFT calculations suggest that the incorporation of Cu onto the Zn surface lowers the reaction energy (from 0.44 eV to 0.15 eV) of the potential-determining step to form COOH*, which improves CO production rates, while suppressing the HER due to a higher coverage of CO that impedes H adsorption. The changes in these relative energies rationalize the enhanced CO production activity and selectivity of Zn catalysts with Cu modification. Based on our fundamental studies involving planar electrodes, we then prepared a Zn-Cu powder catalyst and integrated it into a vapor-fed reactor. These gas-diffusion electrodes also showed efficient CO_2-to-CO performance at industrially relevant reaction rates, consistent with expectations based on the prior studies. Overall, our work highlights the benefits of rationally designed bimetallic catalyst systems; a constructive ligand effect can modify the electronic properties of the bimetallic surfaces to tune the overall catalytic performance.

Experimental Procedures

Resource Availability. Further information and requests for resources and reagents should be directed to and will be fulfilled by the Lead Contact, Dr. Christopher Hahn (hahn31@llnl.gov). This study did not generate new unique reagents. All data can be found in the Supplemental Information which is available free of charge and can be found on line at Cell Press.

Materials. Zinc foil (99.999%, 0.1mm thick) was purchased from Alfa Aesar; Zinc powder was purchased from Millipore Sigma (particle size 1-5 microns, >99.8%); potassium hydroxide (semiconductor grade, 99.99% metal basis) was purchased from Sigma Aldrich; copper sulfate (99.99%) and hydrochloric acid (35% in water) were purchased from Fisher Scientific; carbon dioxide (99.999%) was purchased from Air Gas. All chemical materials were used without further purification. All electrolyte solutions were prepared by deionized water from the Thermo Scientific Barnstead Nanopure water purification system (18.2 MΩ·cm resistivity).

Preparation of the Zn-Cu electrodes.

Planar electrode. Zn foils were first mechanically polished by 600 grid and 1500 sandpapers, then rinsed by hydrochloric acid and water. The Zn foils were then immersed into a deaerated solution of $CuSO_4$ (10 mM) at room temperature for a period of time (1s - 60s) in order to galvanically exchange the Zn surface by Cu. The resulting foil was then carefully rinsed by water and dried by N_2 gun. The silver color of the Zn foil changed to dark gray after the galvanic treatment.

Thin film-based electrode. The Cu-Zn thin film electrodes were deposited by radio frequency magnetron co-sputtering of Cu and Zn metal targets onto 100 mm-diameter Si wafer with an approximately 170 nm SiO_2 diffusion barrier and 10 nm Ti adhesion layer in a sputter deposition system (Kurt J. Lesker, PVD) with 10^{-5} Pa base pressure. The working atmosphere was composed of 0.8 Pa Ar gas. The substrate holder was rotating at a speed of 5 rpm, and the deposition proceeded for 8 min with no intentional substrate heating. The powers applied on Cu and Zn sources were adjusted to ensure the desired Cu/Zn composition, which was further confirmed by x-ray fluorescence (XRF) measurements using an EDAX Orbis Micro-XRF system. The composition gradient film was deposited similarly but without substrate rotation such that the sputter deposition gradient from each source resulted in a composition library thin film.

Gas diffusion electrode. 1.0 g of Zn powders were added into 10 mL of $CuSO_4$ (10 mM) solution for 5 seconds, followed by quick filtration and rinsing with excess water. The resulted Zn-Cu powders were dried in air. It was then mechanically grinded using a small-size laboratory mortar for 1 minute until a fine and homogeneous powder was obtained. The powder was then suspended as a 10 mg mL^{-1} aqueous ethanol ink supplemented by a perfluorinated sulfonic acid ionomer, Nafion, as a catalyst binder. The Nafion/catalyst ratio was set equal to 8.7 wt.%. The ink was then sonicated for 10 minutes to ensure homogeneous dispersion of the catalyst and ionomer in the ink. 130 µL of the as-prepared ink was then drop-casted onto 1 cm^2 gas-diffusion layers to reach a catalyst loading of 1.3 mg catalyst.cm^{-2}. During the deposition, the gas-diffusion layers were maintained on a 60°C-hot plate to facilitate solvent evaporation. The generated gas-diffusion electrodes, so-called Zn-Cu (powder) GDE, were then immediately tested for their electrochemical performance.

Electrochemical Measurements. A multichannel potentiostat (Bio-Logic VMP3) was used for all the electrochemical measurements in this study. A two compartment electrochemical cell,[36] comprising a typical three-electrode system was used for all the aqueous CO_2R experiments: Zn-based electrodes as working electrodes (5.9 cm^2 geometric area exposed); a platinum foil as the counter electrode; and an Ag/AgCl electrode (Accumet) as the reference electrode. Selemion AMV (AGC Inc.) was introduced as the anion exchange membrane in between the counter and working electrode compartments. A small distance (< 0.5 cm) between the reference and working electrodes was ensured to the electrolyte resistance. Dry CO_2 gas was humidified by $KHCO_3$ solution before flow through the electrochemical cell, with a flow rate of 20 sccm regulated by a mass flow controller (πMFC, MKS Instruments). A 0.1 M solution of $KHCO_3$ saturated with CO_2 (pH = 7.2) was prepared as the electrolyte.

The electrochemical performances of the Zn-Cu GDEs were assessed in a polycarbonate 3-compartment cell additionally comprising a (1) Ni foil as the anode and a (2) leakless Ag/AgCl reference electrode (eDAQ). In each experiment, the Zn-Cu GDE was used as a working electrode with a 1.0 cm^2 geometric area exposed, on one side, to the catholyte and, on the other side, to a stream of gaseous CO_2. 1 M KOH aqueous solutions were employed as both the catholyte and the anolyte and were circulated at 10 mL.min^{-1} in the 6-mL cathodic and anodic compartments, using two auxiliary 25-mL reservoirs. A bipolar membrane (Fumasep FAS-50, FuelCellStore) was used between the two compartments. The CO_2 flow rate was regulated using the mass flow controller and was set to 75 sccm.

CO_2R product analysis. The CO_2 reduction products (CO, hydrogen and formate) were identified and quantified by using the same methods in our previous study.[36] To quantify the concentrations of CO and hydrogen, exhaust gas (1.0 mL) was sent to the gas chromatography (SRI 8610C) from the working electrode compartment of the cell at different times during the electrolysis. The liquid product formate was quantified by using ^{1}H NMR spectroscopy (600 MHz, Varian Inova). All the experiments were repeated 3 times to establish statistical significance for the obtained data (Supplementary Table 1 and 5).

High Throughput catalyst screening. Measurement of 5 Zn-Cu catalyst compositions (and pure Cu for comparison) was performed in a custom recirculating flow cell described previously.[64] Briefly, a 6 mm-diameter thin film from the composition library, over which the composition is constant to within approximately 2-4 at.%, was isolated using an o-ring sealed 3-electrode cell with bipolar membrane (Fumasep). Each 15 min electrolysis experiment was performed in a batch reactor mode where recirculation of electrolyte resulted in rapid concentration of reaction products for analytical quantification. Note that the surface concentration of dissolved CO_2 may be slightly lower than in traditional experiments, and the catalyst is continually exposed to reaction products from prior passes of the electrolyte.

Physical characterizations. The SEM images of the Zn-Cu electrodes were obtained using a FEI XL30 field emission scanning electron microscope. Non-contact atomic force microscopy images were obtained by a Park Systems XE-70 or XE-100 scanning probe microscope equipped with a premounted Park Systems NSC15/Al BS tip and calculated topographical information (*i.e.* surface roughness) using Gwyddion software. The XPS spectra were collected by an SSI SProbe XPS spectrometer, using an incident Al Kα radiation of 1486 eV. The XRD patterns for the Zn-Cu electrodes were obtained using a PANanalytical X'Pert diffractometer with an incident Cu Kα radiation of 1.54056 Å.

X-ray absorption spectroscopy was performed in fluorescence mode with a Canberra 100-pixel Ge solid-state monolith detector at Beamline 11-2 at the Stanford Synchrotron Radiation Lightsource. Both the Cu K-edge and Zn K-edge results were calibrated to a foil reference measured simultaneously with the Zn-Cu bimetallic electrode. XAS results were processed in SixPACK (Sam Webb, SSRL) and the Athena module of the Demeter software package.[65] The lack of a prominent XANES feature at ~9669 eV on the Zn K-edge which has been attributed to the existence of a ZnCu alloy could be due to the high Zn content of the alloy which has been shown to reduce the intensity of this feature. The change in the Zn K-edge spectra edge energy between Zn Foil and Zn-Cu alloys was reported as ~1 eV in prior literature,[54] which is larger than the 0.3 eV observed in these measurements. This can be explained by the limited thickness of the alloy layer (~50-100 nm by XPS) relative to the thickness of the Zn foil substrate resulting in a measured intermediate edge shift between a Zn foil and a pure Zn-Cu material.

XRD characterization of the Zn-Cu composition library was performed using a Bruker DISCOVER D8 diffractometer with Cu Kα radiation from a Bruker IμS source. The x-ray spot size was limited to a 2 mm length scale, over which the composition is constant to within approximately 1-2 at.%.

Computational details. To simulate the above synthesized Zn-rich and Cu-rich Zn-Cu bimetallic catalysts, two stepped Zn-Cu surfaces, *hcp* $Zn_{11}Cu_1$(100) and *fcc* Zn_1Cu_8(211), were constructed from original *hcp* Zn(100) and *fcc* Cu(211) surfaces, respectively, by replacing a certain fraction of the step atoms with other metal atoms (Supplementary Fig. 15). Step atoms were selected for replacement due to their low cohesive energies and the Zn:Cu ratio was set to be close to the experimental values. Pure *fcc* metal (211) surfaces and *hcp* Zn(100) surfaces were also simulated for comparison. Adsorption energies were calculated using DFT with a periodic plane-wave implementation and ultra-soft pseudopotentials using the QUANTUM ESPRESSO code,[66] interfaced with the Atomistic Simulation Environment (ASE).[67] We applied the BEEF-vdW functional, which provides a reasonable description of van der Waals forces while maintaining an accurate prediction of chemisorption energies.[68] Plane-wave and density cutoffs were 500 and 5000 eV, respectively, with a Fermi-level smearing width of 0.1 eV. In general, the adsorption energies on *fcc* (211) surfaces were evaluated using four-metal-layer (3 × 1) supercells with the bottom two metal layers constrained and a vacuum layer of 20 Å, and (4 × 4 × 1) Monkhorst-Pack k-point grids were used;[69] while for *hcp* (100) surfaces, four-metal-layer (3 × 2) supercells with the bottom two metal layers constrained and a vacuum layer of 20 Å, and (4 × 3 × 1) Monkhorst-Pack k-point grids were used. For the density of states (DOS) calculation, (8 × 8 × 1) and (8 × 6 × 1) Monkhorst-Pack k-point grids[69] were used for the *fcc* (211) and *hcp* (100) surfaces, respectively. All structures were optimized until the force components were less than 0.05 eV $Å^{-1}$. A dipole correction was applied to decouple the electrostatic interaction between the periodically repeated slabs. The free energy of H_2(g) was corrected by + 0.09 eV as reported by Studt. *et al.*[70] The free energy of CO_2(g) was corrected by +0.33 eV to address the overestimation of CO_2 adsorption energies in DFT. Based on previous analysis,[71,72] the solvation energetic corrections of −0.25 eV and −0.06 eV were considered for COOH* and CO*, respectively.

The adsorption energies present in Figure 4, Figure S13, and Figure S14 are defined as:

$$\Delta G_{\mathrm{ads}}^{\mathrm{COOH*}} = \mu(\mathrm{slab + COOH*}) - \mu(\mathrm{slab}) - \mu(\mathrm{CO_2}) - \frac{1}{2}\mu(\mathrm{H_2}) \tag{1}$$

$$\Delta G_{\mathrm{ads}}^{\mathrm{CO*}} = \mu(\mathrm{slab + CO*}) + \mu(\mathrm{H_2O}) - \mu(\mathrm{slab}) - \mu(\mathrm{CO_2}) - \mu(\mathrm{H_2}) \tag{2}$$

$$\Delta G_{\mathrm{ads}}^{\mathrm{H*}} = \mu(\mathrm{slab} + \mathrm{H*}) - \mu(\mathrm{slab}) - \frac{1}{2}\mu(\mathrm{H}_2) \tag{3}$$

The free energy corrections to each species are shown in Table S4. The CO and OH adsorption energies present in Figure S12 are obtained on Cu(211) and Zn(100) and defined as:

$$\Delta E_{\mathrm{ads}}^{\mathrm{CO*}} = E(\mathrm{slab} + \mathrm{CO*}) - E(\mathrm{slab}) - E(\mathrm{CO}) \tag{4}$$

$$\Delta E_{\mathrm{ads}}^{\mathrm{OH*}} = E(\mathrm{slab} + \mathrm{OH*}) + \frac{1}{2}E(\mathrm{H}_2) - E(\mathrm{slab}) - E(\mathrm{H}_2\mathrm{O}) \tag{5}$$

All energies of relaxed structures are listed in the Supporting Information as well hosted online at the Catalysis-Hub repository[73] under https://www.catalysis-hub.org/publications/WangSyneristic2020.

Acknowledgements

The galvanic exchange synthesis, physical and electrochemical characterization, and DFT calculations on Zn-Cu bimetallics are based on work performed by the Joint Center for Artificial Photosynthesis, a DOE Energy Innovation Hub, supported through the Office of Science of the U.S. Department of Energy under Award Number DE-SC0004993. Combinatorial high throughput measurements of sputtered Cu-Zn catalysts are based on work performed by the Liquid Sunlight Alliance, which is supported by the U.S. Department of Energy, Office of Science, Office of Basic Energy Sciences, Fuels from Sunlight Hub under Award Number DE-SC0021266. Part of this work was performed at the Stanford Nano Shared Facilities (SNSF), supported by the National Science Foundation under Award ECCS-1542152. Use of the Stanford Synchrotron Radiation Lightsource, SLAC National Accelerator Laboratory, is supported by the U.S. Department of Energy, Office of Science, Office of Basic Energy Sciences under Contract No. DE-AC02-76SF00515. Additional thanks go to the Stanford NMR Facility. L.W. thanks the Knut & Alice Wallenberg Foundation for the financial support, and National University of Singapore and Ministry of Education in Singapore for its financial support through Tier-1 projects with grant numbers R-279-000-622-133 and R-279-000-622-731.

Author Contributions

Conceptualization, L.W., T.F.J, and C.H.; Methodology, L.W., H.P., S.L., Z.Q., D.K., M.B.S., J.A.Z.Z., D.W., L.K., L.Z., and Y.L.; Investigation, L.W., H.P., S.L., Z.Q., D.K., M.B.S., J.A.Z.Z., D.W., L.K., L.Z., Y.L. and M.F.; Writing – Original Draft, L.W, H.P. and S.L.; Writing – Review & Editing, L.W., H.P., S.L., Z.Q., D.K., M.B.S., J.A.Z.Z., D.W., L.K., L.Z., Y.L., M.F., J.G., F.A-P., T.J.F., and C.H.; Funding Acquisition, J.G., F.A-P., T.J.F., and C.H; Supervision, J.G., F.A-P., T.J.F., and C.H.

Declaration of interests

The authors declare no competing interests.

References:

1. Rostrup-Nielsen, J.R., Sehested, J., and Nørskov, J.K. (2002). Hydrogen and Synthesis Gas by Steam- and CO2 Reforming. Adv. Catal. *47*, 65–139.

2. Luk, H.T., Mondelli, C., Ferré, D.C., Stewart, J.A., and Pérez-Ramírez, J. (2017). Status and prospects in higher alcohols synthesis from syngas. Chem. Soc. Rev. *46*, 1358–1426.

3. Haas, T., Krause, R., Weber, R., Demler, M., and Schmid, G. (2018). Technical photosynthesis involving CO2 electrolysis and fermentation. Nat. Catal. *1*, 32–39.

4. Energy Technology Systems Analysis Programme (2010). Syngas Prod. from Coal, http://large.stanford.edu/courses/2013/ph241/kall.

5. Peter, S.C. (2018). Reduction of CO2 to Chemicals and Fuels: A Solution to Global Warming and Energy Crisis. ACS Energy Lett. *3*, 1557–1561.

6. Davis, S.J., Lewis, N.S., Shaner, M., Aggarwal, S., Arent, D., Azevedo, I.L., Benson, S.M., Bradley, T., Brouwer, J., Chiang, Y., et al. (2018). Net-zero emissions energy systems. Science (80-.). *360*, 1419.

7. Jouny, M., Luc, W., and Jiao, F. (2018). General Techno-Economic Analysis of CO 2 Electrolysis Systems.

8. Chen, Y., Li, C.W., and Kanan, M.W. (2012). Aqueous CO2 Reduction at Very Low Overpotential on Oxide-Derived Au Nanoparticles. J. Am. Chem. Soc. *134*, 19969–19972.

9. Liu, M., Pang, Y., Zhang, B., De Luna, P., Voznyy, O., Xu, J., Zheng, X., Dinh, C.T., Fan, F., Cao, C., et al. (2016). Enhanced electrocatalytic CO2 reduction via field-induced reagent concentration. Nature *537*, 382–386.

10. Yoon, Y., Hall, A.S., and Surendranath, Y. (2016). Tuning of Silver Catalyst Mesostructure Promotes Selective Carbon Dioxide Conversion into Fuels. Angew. Chemie - Int. Ed. *55*, 15282–15286.

11. Ma, M., Trześniewski, B.J., Xie, J., and Smith, W.A. (2016). Selective and Efficient Reduction of Carbon Dioxide to Carbon Monoxide on Oxide-Derived Nanostructured Silver Electrocatalysts. Angew. Chemie - Int. Ed. *55*, 9748–9752.

12. Zhu, W., Michalsky, R., Metin, Ö., Lv, H., Guo, S., Wright, C.J., Sun, X., Peterson, A.A., and Sun, S. (2013). Monodisperse Au nanoparticles for selective electrocatalytic reduction of CO2 to CO. J. Am. Chem. Soc. *135*, 16833–16836.

13. Lu, Q., Rosen, J., Zhou, Y., Hutchings, G.S., Kimmel, Y.C., Chen, J.G., and Jiao, F. (2014). A selective and efficient electrocatalyst for carbon dioxide reduction. Nat. Commun. *5*, 1–6.

14. Wang, Y., Cao, L., Libretto, N.J., Li, X., Li, C., Wan, Y., He, C., Lee, J., Gregg, J., Zong, H., et al. (2019). Ensemble Effect in Bimetallic Electrocatalysts for CO2 Reduction. J. Am. Chem. Soc. *141*, 16635–16642.

15. He, J., Dettelbach, K.E., Huang, A., and Berlinguette, C.P. (2017). Brass and Bronze as Effective CO2Reduction Electrocatalysts. Angew. Chemie - Int. Ed. *56*, 16579–16582.

16. Rasul, S., Anjum, D.H., Jedidi, A., Minenkov, Y., Cavallo, L., and Takanabe, K. (2015). A highly selective copper-indium bimetallic electrocatalyst for the electrochemical reduction of aqueous CO2to CO. Angew. Chemie - Int. Ed. *54*, 2146–2150.

17. Yin, Z., Gao, D., Yao, S., Zhao, B., Cai, F., Lin, L., Tang, P., Zhai, P., Wang, G., Ma, D., et al. (2016). Highly selective palladium-copper bimetallic electrocatalysts for the electrochemical reduction of CO 2 to CO. Nano Energy *27*, 35–43.

18. Sun, K., Cheng, T., Wu, L., Hu, Y., Zhou, J., Maclennan, A., Jiang, Z., Gao, Y., Goddard, W.A., and Wang,

Z. (2017). Ultrahigh Mass Activity for Carbon Dioxide Reduction Enabled by Gold-Iron Core-Shell Nanoparticles. J. Am. Chem. Soc. *139*, 15608–15611.

19. Lamaison, S., Blanchard, J., Giaume, D., Fontecave, M., Lamaison, S., Wakerley, D., Blanchard, J., and Montero, D. (2020). High-Current-Density CO 2 -to-CO Electroreduction on Ag-Alloyed Zn Dendrites at Elevated Pressure. Joule *4*, 395–406.

20. Sarfraz, S., Garcia-Esparza, A.T., Jedidi, A., Cavallo, L., and Takanabe, K. (2016). Cu-Sn Bimetallic Catalyst for Selective Aqueous Electroreduction of CO2to CO. ACS Catal. *6*, 2842–2851.

21. Kim, D., Resasco, J., Yu, Y., Asiri, A.M., and Yang, P. (2014). Synergistic geometric and electronic effects for electrochemical reduction of carbon dioxide using gold–copper bimetallic nanoparticles. Nat. Commun. *5*, ncomms5948.

22. Lamaison, S., Wakerley, D., Montero, D., Taverna, D., Giaume, D., Mercier, D., Blanchard, J., and Tran, N. (2019). Zn – Cu Alloy Nanofoams as Efficient Catalysts for the Reduction of CO 2 to Syngas Mixtures with a Potential- Independent H 2 / CO Ratio. ChemSusChem, 511–517.

23. Hori, Y., Murata, A., and Ito, S. (1990). Enhanced Evolution of CO and Suppressed Formation of Hydrocarbons in Electroreduction of CO2 at a Copper Electrode Modified with Cadmium. Chem. Lett., 1231–1234.

24. Li, Q., Fu, J., Zhu, W., Chen, Z., Shen, B., Wu, L., and Xi, Z. (2017). Tuning Sn-Catalysis for Electrochemical Reduction of CO 2 to CO via the Core/Shell Cu/SnO 2 Structure. *139*, 4290–4293.

25. Hu, X.M., Hval, H.H., Bjerglund, E.T., Dalgaard, K.J., Madsen, M.R., Pohl, M.M., Welter, E., Lamagni, P., Buhl, K.B., Bremholm, M., et al. (2018). Selective CO2 Reduction to CO in Water using Earth-Abundant Metal and Nitrogen-Doped Carbon Electrocatalysts. ACS Catal. *8*, 6255–6264.

26. Jiang, K., Siahrostami, S., Zheng, T., Hu, Y., Hwang, S., Stavitski, E., Peng, Y., Dynes, J., Gangisetty, M., Su, D., et al. (2018). Isolated Ni single atoms in graphene nanosheets for high-performance CO2 reduction. Energy Environ. Sci. *11*, 8–14.

27. Li, X., Bi, W., Chen, M., Sun, Y., Ju, H., Yan, W., Zhu, J., Wu, X., Chu, W., Wu, C., et al. (2017). Exclusive Ni − N 4 Sites Realize Near-Unity CO Selectivity for Electrochemical CO 2 Reduction. J. Am. Chem. Soc. *139*, 14889–14892.

28. Koshy, D.M., Chen, S., Lee, D.U., Stevens, M.B., Abdellah, A.M., Dull, S.M., Chen, G., Nordlund, D., Gallo, A., Hahn, C., et al. (2020). Understanding the Origin of Highly Selective CO 2 Electroreduction to CO on Ni , N-doped Carbon Catalysts Forschungsartikel. Angew. Chem. Int. Ed. *132*, 4072–4079.

29. Pan, Y., Lin, R., Chen, Y., Liu, S., Zhu, W., Cao, X., Chen, W., Wu, K., Cheong, W., Wang, Y., et al. (2018). Design of Single-Atom Co − N 5 Catalytic Site: A Robust Electrocatalyst for CO 2 Reduction with Nearly 100% CO Selectivity and Remarkable Stability. J. Am. Chem. Soc. *148*, 4218–4221.

30. Yang, H. Bin, Hung, S.F., Liu, S., Yuan, K., Miao, S., Zhang, L., Huang, X., Wang, H.Y., Cai, W., Chen, R., et al. (2018). Atomically dispersed Ni(i) as the active site for electrochemical CO2 reduction. Nat. Energy *3*, 140–147.

31. Huan, T.N., Ranjbar, N., Rousse, G., Sougrati, M., Zitolo, A., Mougel, V., Jaouen, F., and Fontecave, M. (2017). Electrochemical Reduction of CO2 Catalyzed by Fe-N-C Materials: A Structure-Selectivity Study. ACS Catal. *7*, 1520–1525.

32. Ren, S., Joulié, D., Salvatore, D., Torbensen, K., Wang, M., Robert, M., and Berlinguette, C.P. (2019). Molecular electrocatalysts can mediate fast, selective CO2 reduction in a flow cell. Science (80-.). *365*, 367–369.

33. Lin, S., Diercks, C.S., Zhang, Y., Kornienko, N., Yaghi, O.M., and Chang, C.J. (2015). Covalent organic

frameworks comprising cobalt porphyrins for catalytic CO 2 reduction in water. Science (80-.). *349*, 1208–1212.

34. Zhang, X., Wu, Z., Zhang, X., Li, L., Li, Y., Xu, H., Li, X., and Yu, X. (2017). Highly selective and active CO 2 reduction electro- catalysts based on cobalt phthalocyanine/carbon nanotube hybrid structures. Nat. Commun. *8*, ncomms14675.

35. Zhanaidarova, A., Jones, S.C., Despagnet-Ayoub, E., Pimentel, B.R., and Kubiak, C.P. (2019). Re(tBu-bpy)(CO) 3 Cl Supported on Multi-Walled Carbon Nanotubes Selectively Reduces CO 2 in Water. J. Am. Chem. Soc. *141*, 17270–17277.

36. Wang, L., Nitopi, S.A., Wong, A.B., Snider, J.L., Nielander, A.C., Morales-guio, C.G., Orazov, M., Higgins, D.C., Hahn, C., and Thomas, F. (2019). Electrochemically converting carbon monoxide to liquid fuels by directing selectivity with electrode surface area. Nat. Catal. *2*, 702–708.

37. Talanquer, V., Oxtoby, D., Islam, M.F., Zhang, J., Collings, P.J., Yodh, A.G., Gleiter, H., Perepezko, J., Terrones, M., Dwyer, J.R., et al. (2012). Molecular Fe Catalyst. Science (80-.). *338*, 90–94.

38. Kaminsky, C.J., Wright, J., and Surendranath, Y. (2019). Graphite-Conjugation Enhances Porphyrin Electrocatalysis. ACS Catal. *9*, 3667–3671.

39. Noda, H., Ikeda, S., Oda, Y., Imai, K., Maeda, M., Ito, K., Ideka, S., Oda, Y., Imai, K., Maeda, M., et al. (1990). Electrochemical reduction of carbon dioxide at various metal electodes in aqueous potassium hydrogen carbonate solution. Bull. Chem. Soc. Jpn. *63*, 2459–2462.

40. Kuhl, K.P., Hatsukade, T., Cave, E.R., Abram, D.N., Kibsgaard, J., and Jaramillo, T.F. (2014). Electrocatalytic conversion of carbon dioxide to methane and methanol on transition metal surfaces. J. Am. Chem. Soc. *136*, 14107–14113.

41. Hori, Y. (2008). Electrochemical CO 2 Reduction on Metal Electrodes. Mod. Asp. Electrochem., 89–189.

42. Peterson, A., and Nørskov, J. (2012). Activity Descriptors for CO2 Electroreduction to Methane on Transition - Metal Catalysts. J. Phys. Chem. Lett. *3*, 251–258.

43. Ren, D., Ang, B.S.H., and Yeo, B.S. (2016). Tuning the Selectivity of Carbon Dioxide Electroreduction toward Ethanol on Oxide-Derived CuxZn Catalysts. ACS Catal. *6*, 8239–8247.

44. Abe, H., and Miyauchi, M. (2017). Selective electro- or photo-reduction of carbon dioxide to formic acid using a Cu–Zn alloy catalyst. J. Mater. Chem. A *5*, 12113–12119.

45. Feng, Y., Li, Z., Liu, H., Dong, C., Wang, J., Kulinich, S.A., and Du, X. (2018). Laser-Prepared CuZn Alloy Catalyst for Selective Electrochemical Reduction of CO2 to Ethylene. Langmuir *34*, 13544–13549.

46. Ren, D., Gao, J., Pan, L., Wang, Z., Luo, J., Zakeeruddin, S.M., Hagfeldt, A., and Grätzel, M. (2019). Atomic Layer Deposition of ZnO on CuO Enables Selective and Efficient Electroreduction of Carbon Dioxide to Liquid Fuels. Angew. Chemie - Int. Ed. *58*, 15036–15040.

47. Wichern, C.M., De Cooman, B.C., and Van Tyne, C.J. (2004). Surface roughness changes on a hot-dipped galvanized sheet steel during deformation at low strain levels. Acta Mater. *52*, 1211–1222.

48. Bard, A.J., and Larry R. Faulkner (2001). Electrochemical Methods: Fundamentals and Applications.

49. Zuo, J., and Erbe, A. (2010). Optical and electronic properties of native zinc oxide films on polycrystalline Zn. Phys. Chem. Chem. Phys. *12*, 11467–11476.

50. Sankar, R., Navaneethan, M., Mani, G.K., Ponnusamy, S., Tsuchiya, K., Muthamizhchelvan, C., Kawasaki, S., and Hayakawa, Y. (2016). Influence of Al doping on the structural , morphological , optical , and gas sensing properties of ZnO nanorods In fl uence of Al doping on the structural , morphological , optical , and

gas sensing properties of ZnO nanorods. J. Alloys Compd. *698*, 555–564.

51. Timoshenko, J., Jeon, H.S., Sinev, I., Haase, F.T., Herzog, A., and Roldan Cuenya, B. (2020). Linking the evolution of catalytic properties and structural changes in copper–zinc nanocatalysts using operando EXAFS and neural-networks. Chem. Sci. *11*, 3727–3736.

52. Luo, W., Zhang, Q., Zhang, J., Moioli, E., Zhao, K., and Züttel, A. (2020). Electrochemical reconstruction of ZnO for selective reduction of CO2 to CO. Appl. Catal. B Environ. *273*, 119060.

53. Espinós, J.P., Morales, J., Barranco, A., Caballero, A., Holgado, J.P., and González-Elipe, A.R. (2002). Interface effects for Cu, CuO, and Cu2O deposited on SiO2 and ZrO2. XPS determination of the valence state of copper in Cu/SiO2 and Cu/ZrO2 catalysts. J. Phys. Chem. B *106*, 6921–6929.

54. Yeh, H.C., and Azároff, L. V. (1967). X-ray K absorption edges of alloys. III. Copper-zinc and nickel-zinc systems. J. Appl. Phys. *38*, 4034–4038.

55. Hall, A.S., Yoon, Y., Wuttig, A., and Surendranath, Y. (2015). Mesostructure-Induced Selectivity in CO2Reduction Catalysis. J. Am. Chem. Soc. *137*, 14834–14837.

56. Mezzavilla, S., Horch, S., Stephens, I.E.L., Seger, B., and Chorkendorff, I. (2019). Structure Sensitivity in the Electrocatalytic Reduction of CO 2 with Gold Catalysts. Angew. Chemie - Int. Ed. *58*, 3774–3778.

57. Cave, E.R., Shi, C., Kuhl, K.P., Hatsukade, T., Abram, D.N., Hahn, C., Chan, K., and Jaramillo, T.F. (2018). Trends in the Catalytic Activity of Hydrogen Evolution during CO2 Electroreduction on Transition Metals. ACS Catal. *8*, 3035–3040.

58. Landers, A.T., Fields, M., Torelli, D.A., Xiao, J., Hellstern, T.R., Francis, S.A., Tsai, C., Kibsgaard, J., Lewis, N.S., Chan, K., et al. (2018). The Predominance of Hydrogen Evolution on Transition Metal Sulfides and Phosphides under CO2 Reduction Conditions: An Experimental and Theoretical Study. ACS Energy Lett. *3*, 1450–1457.

59. Ringe, S., Morales-Guio, C.G., Chen, L.D., Fields, M., Jaramillo, T.F., Hahn, C., and Chan, K. (2020). Double layer charging driven carbon dioxide adsorption limits the rate of electrochemical carbon dioxide reduction on Gold. Nat. Commun. *11*, 10.1038/s41467-019-13777-z.

60. Liu, X., Xiao, J., Peng, H., Hong, X., Chan, K., and Nørskov, J.K. (2017). Understanding trends in electrochemical carbon dioxide reduction rates. Nat. Commun. *8*, ncomms15438.

61. Beverskog, B., and Puigdomenech, I. (1997). Revised pourbaix diagrams for zinc at 25-300°C. Corros. Sci. *39*, 107–114.

62. Mahyoub, S.A., Qaraah, F.A., Chen, C., Zhang, F., Yan, S., and Cheng, Z. (2020). An overview on the recent developments of Ag-based electrodes in the electrochemical reduction of CO2 to CO. Sustain. Energy Fuels *4*, 50–67.

63. Wang, R., Haspel, H., Pustovarenko, A., Dikhtiarenko, A., Russkikh, A., Shterk, G., Osadchii, D., Ould-Chikh, S., Ma, M., Smith, W.A., et al. (2019). Maximizing Ag Utilization in High-Rate CO2 Electrochemical Reduction with a Coordination Polymer-Mediated Gas Diffusion Electrode. ACS Energy Lett. *4*, 2024–2031.

64. Jones, R.J.R., Wang, Y., Lai, Y., Shinde, A., and Gregoire, J.M. (2018). Reactor design and integration with product detection to accelerate screening of electrocatalysts for carbon dioxide reduction. Rev. Sci. Instrum. *89*.

65. Ravel, B., and Newville, M. (2005). ATHENA , ARTEMIS , HEPHAESTUS : data analysis for X-ray absorption spectroscopy using IFEFFIT. J. Synchrotron Radiat. *12*, 537–541.

66. Giannozzi, P., Baroni, S., Bonini, N., Calandra, M., Car, R., Cavazzoni, C., Chiarotti, G.L., Cococcioni, M.,

Dabo, I., Corso, A.D., et al. (2009). QUANTUM ESPRESSO: a modular and open-source software project for quantum simulations of materials. J. Phys. Condens. Matter *21*, 395502.

67. Bahn, S.R., and Jacobsen, K.W. (2002). An object-oriented scripting interface to a legacy electronic structure code. Comput. Sci. Eng. *4*, 56–66.

68. Wellendorff, J., Lundgaard, K.T., Møgelhøj, A., Petzold, V., Landis, D.D., Nørskov, J.K., Bligaard, T., and Jacobsen, K.W. (2012). Density functionals for surface science: Exchange-correlation model development with Bayesian error estimation. Phys. Rev. B *85*, 235149.

69. Monkhorst, H.J., and Pack, J.D. (1976). Special points for Brillouin-zone integrations. Phys. Rev. B *13*, 5188–5192.

70. Studt, F., Behrens, M., Kunkes, E.L., Thomas, N., Zander, S., Tarasov, A., Schumann, J., Frei, E., Varley, J.B., Abild-Pedersen, F., et al. (2015). The Mechanism of CO and CO2 Hydrogenation to Methanol over Cu-Based Catalysts. ChemCatChem *7*, 1105–1111.

71. Peterson, A.A., Abild-Pedersen, F., Studt, F., Rossmeisl, J., and Nørskov, J.K. (2010). How copper catalyzes the electroreduction of carbon dioxide into hydrocarbon fuels. Energy Environ. Sci. *3*, 1311.

72. Ludwig, T., Gauthier, J.A., Brown, K.S., Ringe, S., Nørskov, J.K., and Chan, K. (2019). Solvent–Adsorbate Interactions and Adsorbate-Specific Solvent Structure in Carbon Dioxide Reduction on a Stepped Cu Surface. J. Phys. Chem. C *123*, 5999–6009.

73. Winther, K.T., Hoffmann, M.J., Boes, J.R., Mamun, O., Bajdich, M., and Bligaard, T. (2019). Catalysis-Hub.org, an open electronic structure database for surface reactions. Sci. Data *6*, 75.